Volume 11
Number 11
7 June 2024
Pages 2531–2762

Materials Horizons

rsc.li/materials-horizons

ISSN 2051-6347

ROYAL SOCIETY OF CHEMISTRY

COMMUNICATION

Hu Zhang *et al.*

Excellent thermomagnetic power generation for harvesting waste heat *via* a second-order ferromagnetic transition

10 YEARS ANNIVERSARY

Materials Horizons

ROYAL SOCIETY OF CHEMISTRY

COMMUNICATION

View Article Online
View Journal | View Issue

Cite this: *Mater. Horiz.*, 2024, 11, 2603

Received 25th December 2023,
Accepted 28th March 2024

DOI: 10.1039/d3mh02225k

rsc.li/materials-horizons

Excellent thermomagnetic power generation for harvesting waste heat *via* a second-order ferromagnetic transition†

Haodong Chen,[a] Xianliang Liu,[a] Yao Liu,[b] Longlong Xie,[a] Ziyuan Yu,[a] Kaiming Qiao,[a] Mingze Liu,[a] Fengxia Hu,[c] Baogen Shen,[c] R. V. Ramanujan,[d] Ke Chu[e] and Hu Zhang *[a]

Thermomagnetic generation (TMG), a promising technology to convert low-grade waste heat to electricity, utilizes high performance TMG materials. However, the drawbacks of large hysteresis, poor mechanical properties and inadequate service life hinder the practical applications. For the first time, we evaluated the effect of different phase transitions on the TMG performance by systematically comparing the TMG performance of three typical Heusler alloys with similar composition but different phase transitions. $Ni_2Mn_{1.4}In_{0.6}$ exhibits second-order magnetic transition (SOMT) from the ferromagnetic (FM) to paramagnetic (PM) state around T_C = 316 K without thermal hysteresis. It presents highly comprehensive TMG performance, which is not only better than those of other two Heusler alloys with different phase transitions, but also better than those of most typical TMG materials. The maximum power density (1752.3 mW m^{-3}), cost index (2.78 μW per €), and power generation index PGI (8.91 × 10^{-4}) of $Ni_2Mn_{1.4}In_{0.6}$ are 1–5, 1–4, and 1–7 orders of magnitude higher than those of most typical reported materials, respectively. In addition, $Ni_2Mn_{1.4}In_{0.6}$ with SOMT also shows some advantages that first-order magnetic transition (FOMT) materials do not have, such as zero hysteresis and a long-term service life. In contrast to the short lifetime of a few minutes for the materials with FOMT, $Ni_2Mn_{1.4}In_{0.6}$ with SOMT can serve for one month or even longer with excellent cycling stability. Consequently, we conclude that the SOMT $Ni_2Mn_{1.4}In_{0.6}$ Heusler alloy with good TMG performance as well as zero hysteresis and long service life can be a better candidate than FOMT materials for practical applications of TMG.

New concepts

Unlike most of the previous works which emphasized that first-order magnetic transition (FOMT) materials are good candidates for thermomagnetic generation (TMG), for the first time, we systematically compared three typical Heusler alloys in the same system with similar composition but different phase transitions in the TMG working temperature range. Furthermore, we also proposed a new comparison parameter (PGI), which can eliminate the comparison errors caused by various non-intrinsic factors. The maximum power density $P_{D\text{-}max}$ (1752.3 mW m^{-3}), cost index C_0 (2.78 μW per €), and PGI (8.91 × 10^{-4}) of $Ni_2Mn_{1.4}In_{0.6}$ are 1–5, 1–4, and 1–7 orders of magnitude higher than those of most typical reported materials, respectively. In particular, we compared the service life of materials with different phase transitions based on a cycle life test device (Fig. 4(d)). In contrast to the short lifetime of a few minutes for the materials with FOMT, NiMnIn with second-order magnetic transition (SOMT) can serve for one month or even longer with excellent cycle stability. Consequently, good TMG performance with zero hysteresis as well as a long-term service life make us conclude that SOMT NiMnIn Heusler alloys would be better candidates for practical applications of TMG.

1. Introduction

Waste heat is produced in most energy conversion systems,[1] such as materials processing and transportation.[2] According to the temperature range, waste heat can be classified as high-grade (>650 °C), medium-grade (230–650 °C), and low-grade (<230 °C).[3] The low-grade type accounts for 63% of the total

[a] School of Materials Science and Engineering, University of Science and Technology of Beijing, Beijing 100083, P. R. China. E-mail: zhanghu@ustb.edu.cn; Tel: +86-10-62333733
[b] Frontier Institute of Science and Technology, Xi'an Jiaotong University, Xi'an 710049, P. R. China. E-mail: liuyao12@xjtu.edu.cn
[c] Beijing National Laboratory for Condensed Matter Physics, Institute of Physics, Chinese Academy of Sciences, Beijing 100190, P. R. China. E-mail: fxhu@iphy.ac.cn, shenbg@iphy.ac.cn
[d] School of Materials Science and Engineering, Nanyang Technological University, Singapore 639798, Singapore. E-mail: Ramanujan@ntu.edu.sg
[e] School of Materials Science and Engineering, Lanzhou Jiaotong University, Lanzhou 730070, P. R. China. E-mail: chukelut@163.com
† Electronic supplementary information (ESI) available. See DOI: https://doi.org/10.1039/d3mh02225k

waste heat,[4] but only 6% of this heat is harvested.[5] Some technologies have been reported for waste heat recovery. The thermoelectric generator (TEG), based on the Seebeck effect, is a common waste heat recovery technology, but it has low energy conversion efficiency below 200 °C.[6,7] Organic Rankine cycle (ORC) shows relatively high efficiency in the low-grade temperature range, but the emitted organic matter is harmful to the environment.[8] Besides, liquid state energy harvesting from low enthalpy has also been developed, including thermomagnetic hydrodynamic harvesting,[9] pyroelectric harvesting,[10] and triboelectric harvesting.[11,12] These methods can be applied to microsystems and wearable devices, but the deposition of nanoparticles in magnetic fluids and the difficulty of controlling the liquid hinder their practical applications.[9,11] In contrast, thermomagnetic generation (TMG) is a highly promising technology for low-grade waste heat recovery,[13,14] which can be divided into passive TMG and active TMG. Generally, the passive TMG converts thermal energy into mechanical energy first, and then transfer mechanical energy further into electrical energy, which will generate relatively low current and output power due to the indirect conversion of thermal energy to electrical energy.[15–18] In contrast, the active TMG directly converts the thermal energy into electrical energy by a magnetic flux change through the coil during the temperature-driven phase transition of the thermomagnetic material according to the Faraday's law. Compared with other waste heat harvesting technologies, active TMG has the advantages of a wide service temperature range, high theoretical efficiency, and is environmentally benign.[8,19]

The concept of TMG was first proposed by Tesla[20] and Edison[21] in the late 19th century, but the high Curie temperature (T_C) and low efficiency of the working material (Fe) made it impractical for waste heat recovery. Hence, the key of TMG is to find materials with appropriate T_C and good TMG performance. The ideal TMG material should undergo a sharp magnetization change around T_C, so a large magnetic flux change could be obtained. Since the requirement for such TMG materials is consistent with that for magnetocaloric effect (MCE) materials,[22,23] this has brought strong interest to MCE materials as potential TMG candidates.[3,24–26] Recently, typical MCE materials, including Gd, $Gd_5(Si, Ge)_4$, NiMn-based Heusler alloys, and $La(Fe, Si)_{13}H_y$/In composites, have been reported to have good potential for TMG applications.[3] Srivastava *et al.*[24] demonstrated that the multiferroic Ni–Co–Mn–Sn Heusler alloy, undergoing a first-order magnetic transition (FOMT) from ferromagnetic (FM) austenite to weak-magnetic martensite, has potential application as a TMG material. However, it should be noted that the large thermal hysteresis accompanied by FOMT brings change in the operating temperature during heating and cooling, which causes difficulties in TMG design and degradation of TMG performance.[3,27] Besides, the huge lattice distortion and internal stresses induced by the FOMT lead to mechanical failure, making it difficult for practical application with a long-term service. On the other hand, although the process of second-order magnetic transition (SOMT) is usually not as intense as that of FOMT, due to the absence of large hysteresis and destructive internal stress, SOMT materials are more favorable to device design and can be applied to TMG with small temperature span and long-term service life. Therefore, it is difficult but highly desirable to search for a SOMT material which exhibits good TMG performance as well as zero hysteresis and a long service life.

Recently, NiMn-based Heusler alloys have been reported by multiple research groups as good TMG materials.[3,24,28–30] Besides, Heusler alloys exhibit both SOMT of austenite phase and FOMT between the FM austenite and weak-magnetic martensite phase.[23,31] Therefore, this allows us to make a more reasonable comparison by choosing materials with similar composition in the same system but different phase transitions. In present work, for the first time we systematically compared the TMG performance of materials with different phase transitions based on an active TMG device. We use this TMG device with a traditional magnetic circuit because more data based on the traditional magnetic circuit can be found and it is conducive to processing and replacing different samples.[25,32] Thus, it can eliminate the impact of different TMG designs, and allow us to compare the performance of different materials more reasonably. In order to further rule out the influence of different material systems or significant differences in composition, we chose three typical Heusler alloys in the same system with similar composition but different phase transitions in the TMG working temperature range, that is, $Ni_2Mn_{1.4}In_{0.6}$ (NiMnIn) with SOMT, $Ni_{36}Co_{14}Mn_{35.7}Ti_{14.3}$ (Co14) with mainly FOMT, and $Ni_{37.5}Co_{12.5}Mn_{35}Ti_{15}$ (Co12.5) with both FOMT and SOMT. A systematic comparison has been carried out and it shows that the TMG performance of $Ni_2Mn_{1.4}In_{0.6}$ with SOMT is not only better than those of other two Heusler alloys with different phase transitions, but also better than those of most reported TMG materials.[3,24,27,33–37] In addition, this SOMT $Ni_2Mn_{1.4}In_{0.6}$ also shows some advantages that FOMT materials do not have, such as zero magnetic hysteresis, zero thermal hysteresis, and good cycling stability. This high comprehensive TMG performance with long-term service life proves that NiMnIn with SOMT has high potential for practical TMG applications.

2. Results and discussion

2.1 Active TMG device

Fig. 1(a) shows our lab-built active TMG device with ice water (~273 K) and boiling water (~373 K) as cold and hot sources, respectively. The hot and cold water was pumped to alternatively flow through the sample cabin, with a flow rate of 0.04 L s^{-1}. The pump is controlled by a programmable microcontroller. A 3D printed nylon shell is placed in a hollow cylindrical Halbach permanent magnet which provides a radial magnetic field of ~1 T. Fig. 1(b) shows the top view of the nylon shell, which is divided into "A" and "B" parts. The A-side is the water inlet and the B-side is the water outlet. Fig. 1(c) shows the side view of the nylon shell. The copper cabin passes through the center of the nylon shell, which is wound by 600

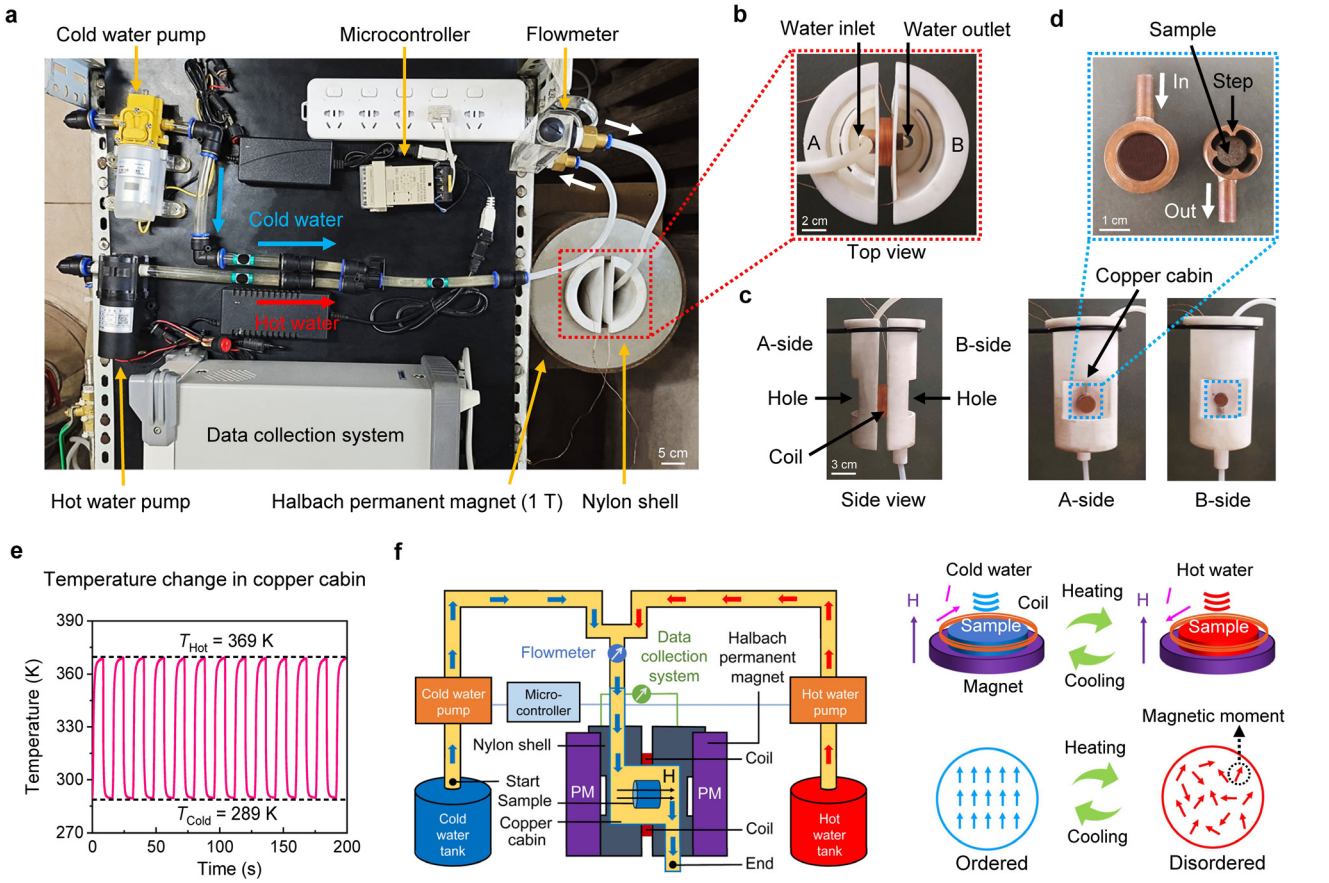

Fig. 1 Structure and working mechanism of the lab-built active TMG device. (a) The image of the TMG device with ice water (~273 K) and boiling water (~373 K) as cold and hot sources, respectively. (b) The top view of the nylon shell, where "A" and "B" represent the two sides of the nylon shell, respectively. (c) The side view of the nylon shell. The copper cabin passes through the center of the nylon shell, which is wound by 600 turns of copper coil. (d) Image of the copper cabin. The copper cabin is connected by two parts, and four steps are cut on the inner wall of the copper cabin. (e) The variation of water temperature in the copper cabin during the TMG cycling. (f) The working mechanism of the present TMG device and the magnetic moment change of the sample during the heating and cooling process.

turns of copper coil. Four steps are cut on the inner wall of the copper cabin (Fig. 1(d)). This design not only ensures the direct heat exchange between the sample and heating/cooling water, but also ensures that the sample is well fixed and not washed away. More importantly, this sample cabin can be easily disassembled through the screw threads, which is conducive to frequent change of different samples. Unlike some other TMGs which need the stacking of many TMG thin plates,[25,32] only a cylindrical bulk sample is needed for this sample cabin. Thus, it greatly reduces the preparation cost and difficulty. The induced electrical signal is collected using a data collection system (RIGOL M300). More details about the TMG device are described in the Experimental section. Fig. 1(e) shows the variation of water temperature during cycling. The water temperature shows a cyclic change between the hot-end and cold-end. The water temperature in the copper cabin reaches ~289 K (cold-end) and ~369 K (hot-end) after passing through the pump and pipe, hence the working temperature range of the TMG device is suitable for harvesting low-grade waste heat.

Fig. 1(f) shows the working mechanism of the TMG device during heating and cooling. When hot water flows through the copper cabin, the sample is heated above its phase transition temperature, so that the magnetic moment changes from the original ordered arrangement along the external magnetic field to a disordered arrangement. Then, the magnetic flux passing through the coil decreases and induces a current in the coil. On the other hand, the cold water causes the sample to undergo a reverse phase transition, and the disordered magnetic moment reverts to an ordered arrangement, resulting in a reverse current in the coil. Since the magnetic flux passing through the coil changes repeatedly due to the repetition of the thermally induced magnetic transition, AC current can be continuously obtained in the coil.

2.2 FOMT and SOMT of Heusler alloys

Fig. 2(a) shows the *in situ* room temperature (RT) synchrotron radiation SXRD patterns of $Ni_{37.5}Co_{12.5}Mn_{35}Ti_{15}$ (Co12.5), $Ni_{36}Co_{14}Mn_{35.7}Ti_{14.3}$ (Co14), and $Ni_2Mn_{1.4}In_{0.6}$ (NiMnIn). Both Co12.5 and Co14 alloys show a two-phase coexistence state of the martensite and austenite phases, suggesting that the martensitic transition of these alloys occurs around RT. The presence of the (220) and (0010) peaks indicates that the

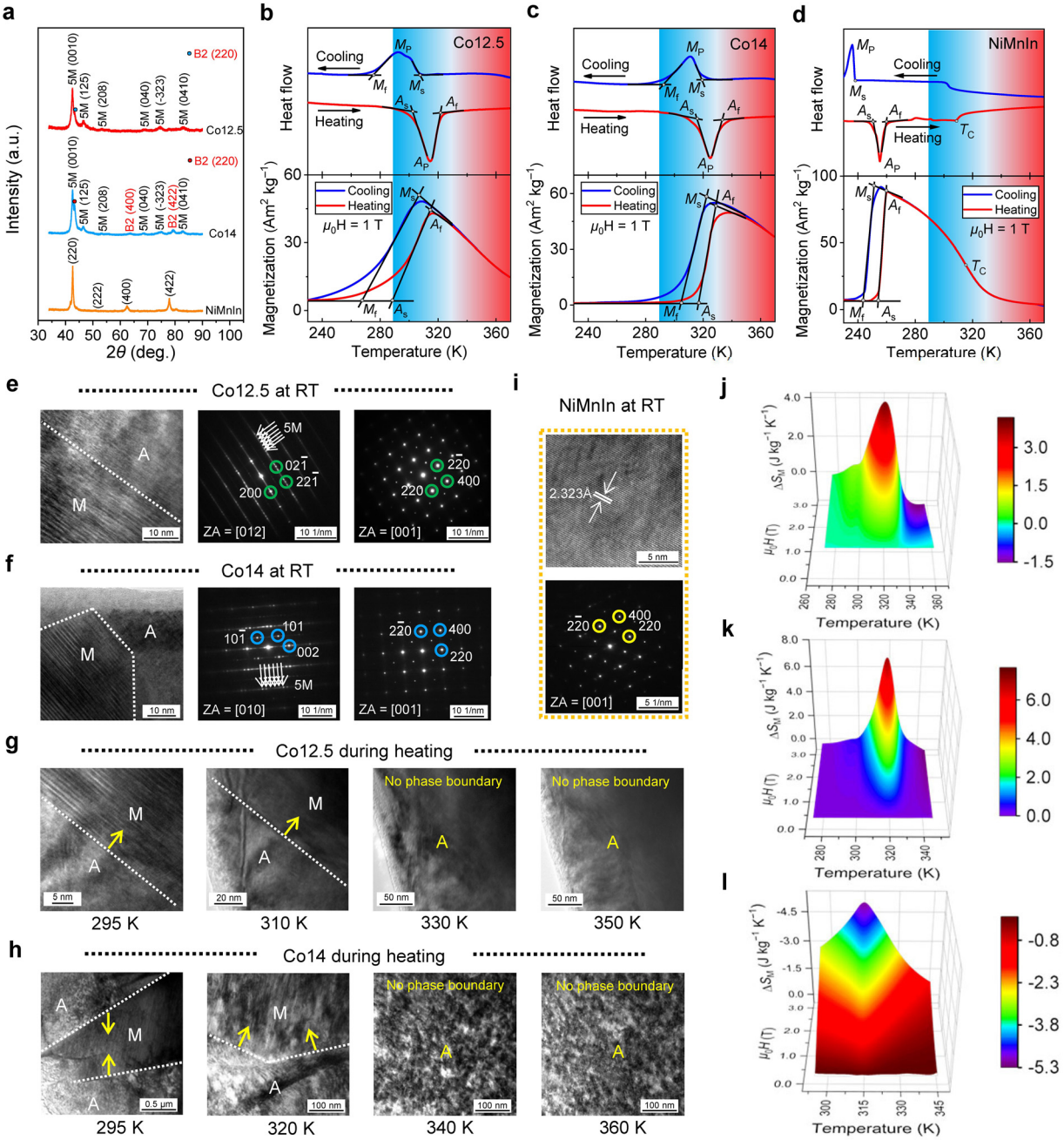

Fig. 2 The microstructure and magnetic properties of Heusler alloys with different phase transitions. (a) Room temperature *in situ* synchrotron radiation X-ray diffraction (SXRD) patterns of $Ni_{37.5}Co_{12.5}Mn_{35}Ti_{15}$ (Co12.5), $Ni_{36}Co_{14}Mn_{35.7}Ti_{14.3}$ (Co14), and $Ni_2Mn_{1.4}In_{0.6}$ (NiMnIn). (b)–(d) The DSC curves in the zero field and *M*–*T* curves under 1 T for (b) Co12.5, (c) Co14, and (d) NiMnIn, respectively. The gradient background from blue to red represents the temperature range from cold-end (289 K) to hot-end (369 K). (e) and (f) High-resolution transmission electron microscopy (HRTEM) and selected area electron diffraction (SAED) images at room temperature for (e) Co12.5 and (f) Co14, respectively. (g) and (h) *In situ* TEM images at different temperatures during the heating process for (g) Co12.5 and (h) Co14, respectively. (i) HRTEM and SAED images for NiMnIn with cubic $L2_1$ austenite at room temperature. (j)–(l) Magnetic entropy change ΔS_M as a function of temperature and magnetic field for (j) Co12.5, (k) Co14, and (l) NiMnIn, respectively.

austenite and martensite are the B2 structure (space group *Fm*3*m*) and 5-layer modulated (5M) structure (space group *P*2/*m*), respectively. On the other hand, NiMnIn is identified to be a single austenite phase with an $L2_1$ structure (space group *Fm*3*m*) at RT. The lattice parameter is a = 6.024 Å.

Fig. 2(b)–(d) show the DSC curves in zero field and the temperature dependence of magnetization (*M*–*T*) curves under 1 T during heating and cooling for all the alloys. The phase transition temperatures and thermal hysteresis (ΔT_{hys}) determined by DSC and *M*–*T* curves are listed in Table 1. All the alloys experience a typical first-order ferromagnetic martensitic transition from FM austenite to weak-magnetic martensite with a ΔT_{hys} of ~20 K. In addition, another second-order FM–PM transition of austenite appears above the martensitic

Table 1 The transition temperatures (K), thermal hysteresis ΔT_{hys} (K) calculated from $\Delta T_{hys} = (A_s + A_f - M_s - M_f)/2$, and magnetic entropy change ΔS_M (J kg^{-1} K^{-1}) for a field change of 0–1 T

	Sample	M_s	M_f	A_s	A_f	T_C	ΔT_{hys}	$\lvert\Delta S_M\rvert$
DSC	Co12.5	307	275	304	322	—	22	—
	Co14	320	295	315	334	—	17	—
	NiMnIn	—	—	—	—	309	—	—
M–T	Co12.5	307	268	288	315	—	14	1.07
	Co14	323	304	317	330	—	10	2.23
	NiMnIn	—	—	—	—	316	—	2.37

transition. Both FOMT and SOMT of Co12.5 occur within the working temperature range, while only the FOMT of Co14 and the SOMT of NiMnIn occur in the working temperature range.

The *M–T* curves reveal that the martensitic transition results in a significant change of magnetization, and the transition becomes sharper with the Co content increasing from Co12.5 to Co14. The magnetization of the parent phase also increases with larger Co content, suggesting that the doping of Co atoms into Ni–Mn–Ti increases the ferromagnetic characteristics of the austenite phase, strengthening the first-order martensitic transition.[38] In addition, due to the presence of large thermal hysteresis (see Table 1), the maximum dM/dT values of FOMT are different during heating and cooling, *e.g.*, the maximum dM/dT of Co12.5 and Co14 during heating reaches 1.7 A m^2 kg^{-1} K^{-1} at 308 K and 4.85 A m^2 kg^{-1} K^{-1} at 324 K, while it is 1.34 A m^2 kg^{-1} K^{-1} at 293 K and 3.61 A m^2 kg^{-1} K^{-1} at 317 K during cooling, respectively (Fig. S1, ESI†). This distinctly different dM/dT and transition temperature of FOMT would lead to a huge inconsistency in the TMG performance during heating and cooling, and a large temperature span that can cover the different transition temperatures during cycling is necessary. In contrast, the SOMT in NiMnIn exhibits a perfectly reversible FM–PM transition in the working temperature range without hysteresis, and so the maximum dM/dT remains at −1.78 A m^2 kg^{-1} K^{-1} during both heating and cooling. Moreover, the magnetization of 90.8 A m^2 kg^{-1} for the NiMnIn parent phase is also higher than the corresponding values of the Co12.5 and Co14 alloys, which results in a larger magnetization change (ΔM) during the phase transition. Larger ΔM indicates a larger energy conversion during the phase transition, which is favorable to the TMG performance.

To further analyze the phase transition process of the FOMT and SOMT, the microstructure of the alloys was characterized by high-resolution transmission electron microscopy (HRTEM). Fig. 2(e) and (f) show the HRTEM and selected area electron diffraction (SAED) images of Co12.5 and Co14 alloys at RT. Both martensite (M) and austenite (A) phases are observed in Co12.5 and Co14 alloys at RT, confirming that their martensitic transition temperature is around RT. The SAED patterns further reveal the martensite with a monoclinic 5M modulation structure as well as austenite with a B2 cubic Heusler structure, respectively (Fig. S2, ESI†). The specific packing-mediated structure indicates a lattice mismatch between the austenite and the martensite,[39] which leads to poor geometric compatibility at the phase boundary during repetitive martensite transitions, and then degrades the mechanical properties of the FOMT materials.

Fig. 2(g) and (h) show the *in situ* TEM images during heating for the Co12.5 and Co14 alloys, respectively. They both show a two-phase coexistence state of martensite and austenite at 295 K. The austenite phase expands with an increase of temperature and phase boundary shifts towards the martensite phase, suggesting a FOMT from the martensite to austenite phase. Martensite disappears and only the austenite phase can be found when the temperature reaches 330 K for Co12.5 and 340 K for Co14 alloys, respectively, revealing the completion of the phase transition. With a further increase of temperature, the austenite undergoes a FM–PM magnetic transition. However, there is no distinct change of microstructure as shown in TEM images, confirming its SOMT nature.

The HRTEM image of NiMnIn at RT is shown in Fig. 2(i). Evenly arranged atomic layers with an interplanar spacing of 2.323 Å can be observed. The SAED pattern of NiMnIn confirms the austenite characteristic of the cubic $L2_1$ Heusler structure, with a zone axis of [001]. Unlike the case of the first-order ferromagnetic martensitic transition, the SOMT of NiMnIn is not accompanied by a structural transition. Thus, there is no increase in dislocation density and internal stress during SOMT,[40,41] and so the NiMnIn alloy exhibiting a SOMT in the working temperature range shows superior mechanical properties due to the absence of a first-order structural transition, and this advantage will enhance its service life.

The magnetic entropy change (ΔS_M) reflects the change in the ordering of magnetic moments. Therefore, a large ΔS_M suggests good TMG performance. The ΔS_M was calculated based on the *M–H* curves using the Maxwell relationship[42] (Fig. S3 and S4, ESI†), as shown in Fig. 2(j)–(l). Both Co12.5 and Co14 alloys show sharp positive ΔS_M peaks due to the FOMT, and the peak ΔS_M value for a field change of 3 T is 4.17 J kg^{-1} K^{-1} for Co12.5 and 7.66 J kg^{-1} K^{-1} for Co14, respectively. The higher and narrower ΔS_M peak of Co14 suggests that the addition of Co to Ni–Mn–Ti would strengthen the first-order martensitic transition.[38] In addition, a small negative ΔS_M is found after the positive ΔS_M peak in both alloys, which is attributed to the SOMT of austenite.[43]

In comparison with the above two alloys, NiMnIn shows a wider negative ΔS_M peak around the SOMT temperature. Usually, the ΔS_M of SOMT is much lower than that of FOMT. However, the ΔS_M of SOMT in NiMnIn is comparable to that of FOMT in Co12.5 and Co14 alloys, and it is even higher than those of Co12.5 and Co14 alloys at low magnetic fields. For example, the $\lvert\Delta S_M\rvert$ peak of NiMnIn reaches 2.37 J kg^{-1} K^{-1} under 1 T, which is 2.21 and 1.06 times that of Co12.5 (1.07 J kg^{-1} K^{-1}) and Co14 (2.23 J kg^{-1} K^{-1}). Such a large MCE suggests that the SOMT in NiMnIn would show better TMG performance than the FOMT in Co12.5 and Co14 alloys. Furthermore, the maximum field supplied by a permanent magnet is usually lower than 2 T, and the processing challenges and cost will increase drastically with an increase of magnetic field. Therefore, it is desirable to search for materials with high

MCE and TMG performance under a low magnetic field. Our large MCE of SOMT under low magnetic fields fits well with this requirement and shows high potential for practical applications.

2.3 Power generation by FOMT and SOMT

2.3.1 The induced voltage of Heusler alloys. According to Faraday's law, the induced voltage (V) in the coil can be calculated using the following equation:[26]

$$V = -NS\frac{dB}{dt} \quad (1)$$

where N is the number of turns of coil wire, S is the cross-sectional area of the coil, and dB/dt is the magnetic flux change rate. For a specific TMG device, the NS is independent of the TMG material. The V only depends on the term dB/dt, and so V depends on dM/dt (since $B = \mu_0 (H + M)$), which can be rewritten as $(dM/dT)(dT/dt)$. Thus, good TMG performance needs a large magnetization change dM/dT, and a high temperature change dT/dt.[3] In the present work, the dM/dT value of SOMT NiMnIn is close to or even lower than that of FOMT materials (Fig. S1, ESI†). However, as shown in Fig. S5 and S6 (ESI†), NiMnIn alloys show a lower heat capacity C_P and larger thermal conductivity λ than Co12.5 and Co14 alloys. For example, the average λ of the NiMnIn alloy is 14.86 W m^{-1} K^{-1}, higher than those of the Co12.5 alloy (9.56 W m^{-1} K^{-1}) and Co14 alloy (9.39 W m^{-1} K^{-1}). These lower C_P and higher λ make NiMnIn alloy exhibit the fastest temperature change rate dT/dt among these materials, which is beneficial for obtaining a larger V (Fig. S7–S11, ESI†).

Fig. 3(a)–(c) show the experimental and simulation induced V in one cycle and the corresponding M–t, dM/dt–t curves. The induced V within 300 s for all the alloys is shown in Fig. S12 (ESI†). All the samples yield stable AC voltage during continuous TMG cycles. A positive V is generated when the magnetization increases, and a negative V is generated when the

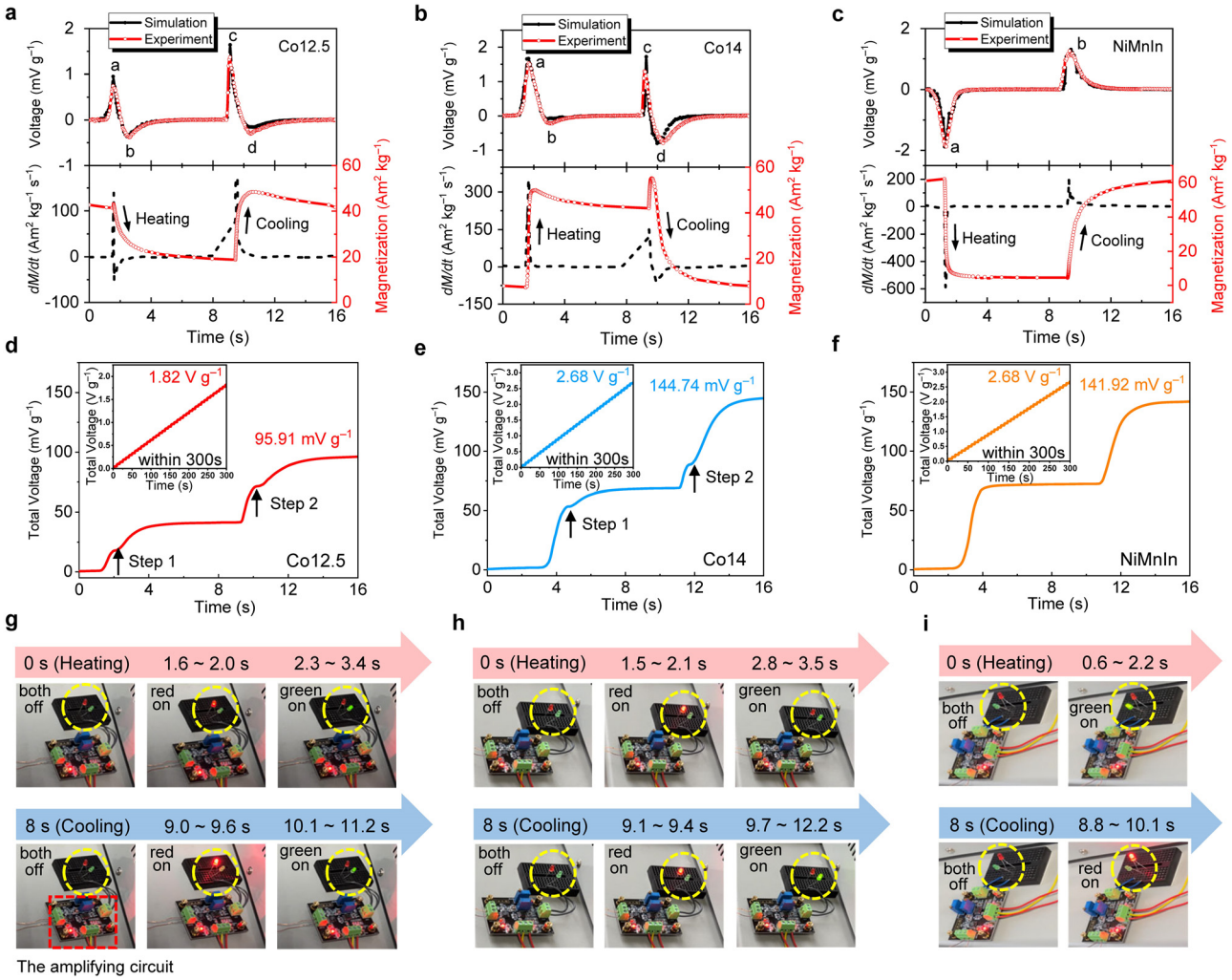

Fig. 3 The experimental and simulation induced voltage V of different alloys, and the experiment of lighting up the LEDs. (a)–(c) The experimental and simulation induced voltage V in one cycle and the corresponding M–t and dM/dt–t curves for (a) Co12.5, (b) Co14, and (c) NiMnIn, respectively. (d)–(f) The total voltage V_{tol} in one cycle for (d) Co12.5, (e) Co14, and (f) NiMnIn, respectively. The inset shows the V_{tol} within 300 s for these alloys. (g)–(i) Time dependence of the OFF and ON states of the LEDs for (g) Co12.5, (h) Co14, and (i) NiMnIn, respectively.

magnetization decreases. Finite element simulations using COMSOL Multiphysics were also performed to study the experimental TMG performance. The detailed process is described in ESI,† Note 6. The simulated V–t curves are in good agreement with the experimental values. A slight discrepancy between the simulation results and experimental data might be attributed to experimental errors and non-ideal thermal conduction in experiments. This good agreement between the experimental and simulation results confirms the reliability of the experimental TMG performance.

Interestingly, both Co12.5 and Co14 generate a large positive V peak followed by a small negative V peak during each heating/cooling cycle, while NiMnIn only generates one V peak in each heating/cooling cycle. Taking Co14 as an example, during heating, the magnetization first increases sharply due to the FOMT from weak-magnetic martensite to FM austenite, resulting in a large dM/dT as well as a positive V peak at point a. Then, the FM austenite will experience a SOMT with a further increase of temperature, which leads to a gradual decrease of M and a small negative V peak at point b. Since the dM/dT and dT/dt during the SOMT are both lower than those during the FOMT, the dM/dt of 348.7 A m^2 kg^{-1} s^{-1} at peak a is significantly larger than that of the dM/dt of −3.4 A m^2 kg^{-1} s^{-1} at peak b, resulting in a higher V peak at a compared to b. During cooling, the Co14 alloy undergoes a reversible SOMT and a first-order martensitic transition. Although the dM/dT during the SOMT is lower than the one during the FOMT, the faster dT/dt at the beginning of the cooling cycle results in a higher dM/dt as well as a larger V peak (at point c) during the SOMT compared to the values (at point d) during the FOMT. Thus, the FOMT with a sharp magnetization change may not show better TMG performance than the SOMT with a less sharp magnetization change. Unlike the MCE that is mainly related to dM/dT, dT/dt also plays an important role in the TMG according to $V \propto (dM/dT)(dT/dt)$.

NiMnIn experiences a reversible SOMT during the heating and cooling processes. Therefore, the dM/dT remains constant, but the T_C = 316 K is closer to the cold-end temperature, hence the magnetic transition occurs earlier during heating than cooling. Accordingly, dT/dt around T_C during heating is larger than that during cooling, leading to a higher dM/dt during heating, *e.g.*, the dM/dt values during heating and cooling are −596.2 A m^2 kg^{-1} s^{-1} (point a) and 190.3 A m^2 kg^{-1} s^{-1} (point b), respectively. This difference in the values of dM/dt results in a difference in the induced V during the heating and cooling processes, and this difference caused by the difference of dT/dt during heating and cooling can be eliminated by shifting the working temperature range such that T_C is in the middle point of the hot-end and the cold-end temperatures.[3] However, in the case of FOMT, since the transition temperatures of FOMT are different during the heating and cooling due to the presence of large hysteresis, this method will lead to a larger difference of dT/dt and V between heating and cooling. Thus, this inconsistency cannot be eliminated by tuning the value of the FOMT transition temperature.

The maximum voltage ($|V_{max}|$) is 0.74, 1.53, and 1.92 mV g^{-1} during heating and 1.37, 1.38, and 1.3 mV g^{-1} during cooling for Co12.5, Co14, and NiMnIn, respectively. It can be seen that, due to the larger magnetization change during the phase transition, lower C_P and higher λ, NiMnIn with SOMT shows the largest $|V_{max}|$ peak among these alloys.

2.3.2 The total voltage of Heusler alloys. Fig. 3(d)–(f) show the total voltage (V_{tol}) in one cycle for all the alloys. The V_{tol} in one cycle of Co12.5, Co14, and NiMnIn reaches 95.91, 144.74, and 141.92 mV g^{-1}, respectively. Two steps are observed in each heating/cooling cycle for Co12.5 and Co14, which is attributed to the successive induced V peaks. The inset shows the V_{tol} within 300 s for Co12.5, Co14, and NiMnIn to be 1.82, 2.68 and 2.68 V g^{-1}, respectively. The TMG properties are contributed only by the SOMT in NiMnIn, while in the case of Co12.5 and Co14 both FOMT and SOMT contribute to the TMG properties. However, NiMnIn shows the highest maximum $|V_{max}|$ and V_{tol} within 300 s among all the alloys. Moreover, the TMG performance of NiMnIn is also significantly better than those of other typical MCE materials, such as Gd,[27] $Ni_{50}Mn_{34}Co_2Sn_{14}$,[3] $Ni_{45}Co_5Mn_{40}Sn_{10}$,[24] $(Mn, Fe)_2(P, As)$,[33] and MM′X (M, M′ = transition metals, X = carbon or boron group elements) alloys.[13] For example, a MM′X alloy with FOMT generated a V_{tol} of 2 V within 65 min with a generation efficiency of 0.031 V min^{-1}.[13] In comparison, our NiMnIn with SOMT produces a V_{tol} of 6.32 V within 5 min with an efficiency of 1.264 V min^{-1}, 40 times higher than that of the MM′X alloy.

2.3.3 Lighting up LEDs. Furthermore, we lit up two LEDs with the assistance of an amplification circuit, so that we can more intuitively analyze the differences of TMG performance caused by different phase transitions through the brightness and duration of LED lights. The specific operations and circuit diagram are described in Fig. S13 (ESI†). The output end of the TMG device was connected to an amplifier circuit, and the voltage regulator circuit with an external power supply was connected to the amplifier circuit to provide the amplifier circuit with the energy required for amplification. Two LEDs in opposite directions were connected in parallel at the output end of the amplifier circuit. Fig. 3(g)–(i) show the time dependence of the OFF and ON states of the LEDs, and the movies of the LED lighting up are provided in Movies S1–S3 (ESI†). The red and green LEDs are driven by positive and negative voltages, respectively. Since Co12.5 and Co14 show successive opposite voltages due to the FOMT and SOMT in each heating/cooling process, the red LED flashes first, followed by the green LED. The brightness of the LEDs varies with the induced voltage. In addition, the duration time of the LEDs is also consistent with the peak width of the induced V. Taking Co14 as an example (Fig. 3(h)), the red LED lit up at 1.5 s when heating, and it lasted for 0.6 s until 2.1 s. This corresponds to the positive a peak in Fig. 3(b). Subsequently, the green LED was turned on by the negative b peak at 2.8–3.5 s. During cooling, the red LED was lit up at 9.1–9.4 s, followed by the lighting up of the green LED at 9.7–12.2 s, which correspond to the c peak and d peak, respectively. As for NiMnIn (Fig. 3(i)), only the green LED was lit up by the negative a peak during heating, and the red LED was lit up by the positive b peak during cooling. However, the relatively high induced V and

wide peak due to the SOMT of NiMnIn make the LEDs brighter and last much longer than the LEDs lit up by the Co12.5 and Co14 alloys.

2.4 Comprehensive service performance

2.4.1 Performance metrics. In order to systematically and comprehensively evaluate the TMG performance of these Heusler alloys, in addition to the measured V value, several other important evaluation metrics, such as energy conversion efficiency (η_{rel}), average power density ($P_{D\text{-}ave}$), and cost index (C_0), have also been taken into account to comprehensively evaluate the TMG performance of different alloys. The value of η_{rel} reflects the ability of TMG materials to convert thermal energy into electric energy, which can be defined as follows:[26]

$$\eta_{rel} = \frac{\eta_{abs}}{\eta_{Carnot}} = \frac{E_{out}}{Q_{in}} \cdot \frac{1}{\eta_{Carnot}} \quad (2)$$

where E_{out} is the net gain electric energy and Q_{in} is the absorbed thermal energy. So, a higher ΔM and a lower Q_{in} (Fig. S14 and S15, ESI†) are favorable for higher η_{rel}. The value of P_D describes the output electric power of a unit volume of the TMG materials.[15,29] The value of C_0 is used to evaluate the output power per unit price,[29,44] which is defined as $P_{D\text{-}max}/C$, where C is the cost of the raw materials (Fig. S16, ESI†).

2.4.2 Effect of different phase transitions on TMG performance. Fig. 4(a) compares the key factors for all three alloys. Due to the high dM/dt caused by excellent thermal properties, NiMnIn generates the largest V_{max} (1.92 mV g^{-1}) among these alloys. Although Co12.5 and Co14 contribute four V peaks in one cycle due to the successive FOMT and SOMT, the V_{tol} within 300 s of 2.68 V for NiMnIn with only SOMT is the same and even larger than those of Co12.5 (1.82 V) and Co14 (2.68 V). Furthermore, NiMnIn has the highest η_{rel} (1.09×10^{-4}%) due to its highest ΔM and the lowest Q_{in}, which is 1.41 and 1.55 times that of Co12.5 (0.8×10^{-4}%) and Co14 (0.74×10^{-4}%). Besides, NiMnIn has the highest $P_{D\text{-}ave}$ (0.50 μW cm^{-3}), which is 3.3 and 1.6 times that of Co12.5 (0.15 μW cm^{-3}) and Co14 (0.32 μW cm^{-3}). This is mainly due to the highest V_{max} and the longer peak duration of NiMnIn (2.8 s during heating and 3.8 s during cooling). Finally, NiMnIn shows a higher C_0 of 2.78 μW per € than that of Co12.5 (1.94 μW per €) and Co14 (2.43 μW per €), which is mainly due to the highest $P_{D\text{-}max}$ of NiMnIn. Overall, NiMnIn shows the best comprehensive TMG performance among these materials.

To investigate the stability and service performance of FOMT and SOMT materials, we carried out a cyclic TMG service test for these alloys. According to the T–t curves in Fig. S9a (ESI†), the sample temperature changes very fast in the first few seconds, and all the phase transitions can be finished within the first 4 s. So, we carried out 450 cycle tests in 30 min with a cycle period of 4 s. Fig. 4(b) shows the time dependence of induced V for these alloys. All the alloys generate an AC voltage during this service. The V_{tol} of NiMnIn is 21.06 V g^{-1}, higher than those of Co12.5 (10.92 V g^{-1}) and Co14 (17.75 V g^{-1}). In addition, the V of Co12.5 and NiMnIn alloys remains nearly constant during the cycling with slight fluctuation, which is mainly caused by heat flow fluctuations of the device and test errors. In comparison, the Co14 alloy exhibits a much higher fluctuation especially after 300 TMG cycles, *e.g.*, the biggest fluctuation reaches as high as 45% (enlarged graph). This is probably due to the appearance of cracks caused by the continuous FOMT, which undermines heat transfer and increases the fluctuation of V_{max}.

Fig. 4(c) shows the surface morphology of Heusler alloys after 450 TMG cycles, and the detailed SEM image is shown in Fig. S17 (ESI†). Co12.5 and NiMnIn show good integrity after long-term service, but Co14 with only FOMT develops obvious cracks. This failure of the Co14 alloy in the long-term service test is verified again by another Co14 sample (Co14-2). The EDS maps show that the elemental distribution at the cracks of the Co14 samples is uniform, indicating that the cracks are not caused by inhomogeneous composition (Fig. S18, ESI†). As mentioned above, a high dislocation density and internal stress due to lattice mismatch will accumulate at the phase boundary during the martensite transition, which would become larger with cycling and result in the final fracture of the FOMT material. In contrast, since Co12.5 only experiences a part of FOMT and NiMnIn undergoes a SOMT in the working temperature range, they present a much better long-term service life without any cracks. To further verify the long-term stability of the SOMT NiMnIn material, we further extended the cycling time to 1 month (120 000 cycles). As shown in Fig. 4(d), we built a cycle life test device. The sample is fixed on the rod of a slide rail, and it can move up and down cyclically. A Peltier patch of ~288 K is placed above as the heat sink, while a constant temperature water bath of ~363 K is placed below as the heat source. The sample will be held for 3 s at each heating/cooling end in order to ensure the completion of the phase transition. This device allows us to test the cycle life of the sample during repeating heating and cooling processes, as shown in Movie S4 (ESI†). It is clearly seen from Fig. 4(e) that the SOMT NiMnIn material shows no cracks and maintains good cycling stability after 0, 1, 2, 3, 7, 14, 21 and 30 days of heating and cooling cycles. We compared the SEM images of the sample surface for the initial state and the one after 30 days (up to 120 000 cycles), and there is no significant difference between them (Fig. S19, ESI†). More importantly, we also obtained the V–t curves of the NiMnIn alloy after 0, 7, 14, 21, and 30 days, respectively, as shown in Fig. S19 (ESI†). It shows that the NiMnIn alloy maintains a very constant TMG performance, proving the excellent cycling stability of the NiMnIn alloy with SOMT. Consequently, in contrast to the short lifetime of a few minutes for the materials with FOMT, the NiMnIn alloy with SOMT can serve for one month or even longer with excellent cycle stability, indicating that SOMT NiMnIn Heusler alloys with zero hysteresis as well as a long-term service life would be better candidates for practical applications of TMG.

2.4.3 Systematic evaluation with classic TMG materials. In order to further prove the good TMG performance of SOMT NiMnIn Heusler alloys, we carried out a comprehensive comparison of the maximum power density $P_{D\text{-}max}$, relative energy conversion efficiency η_{rel}, and cost index C_0 of NiMnIn with SOMT and other typical TMG materials based on the active

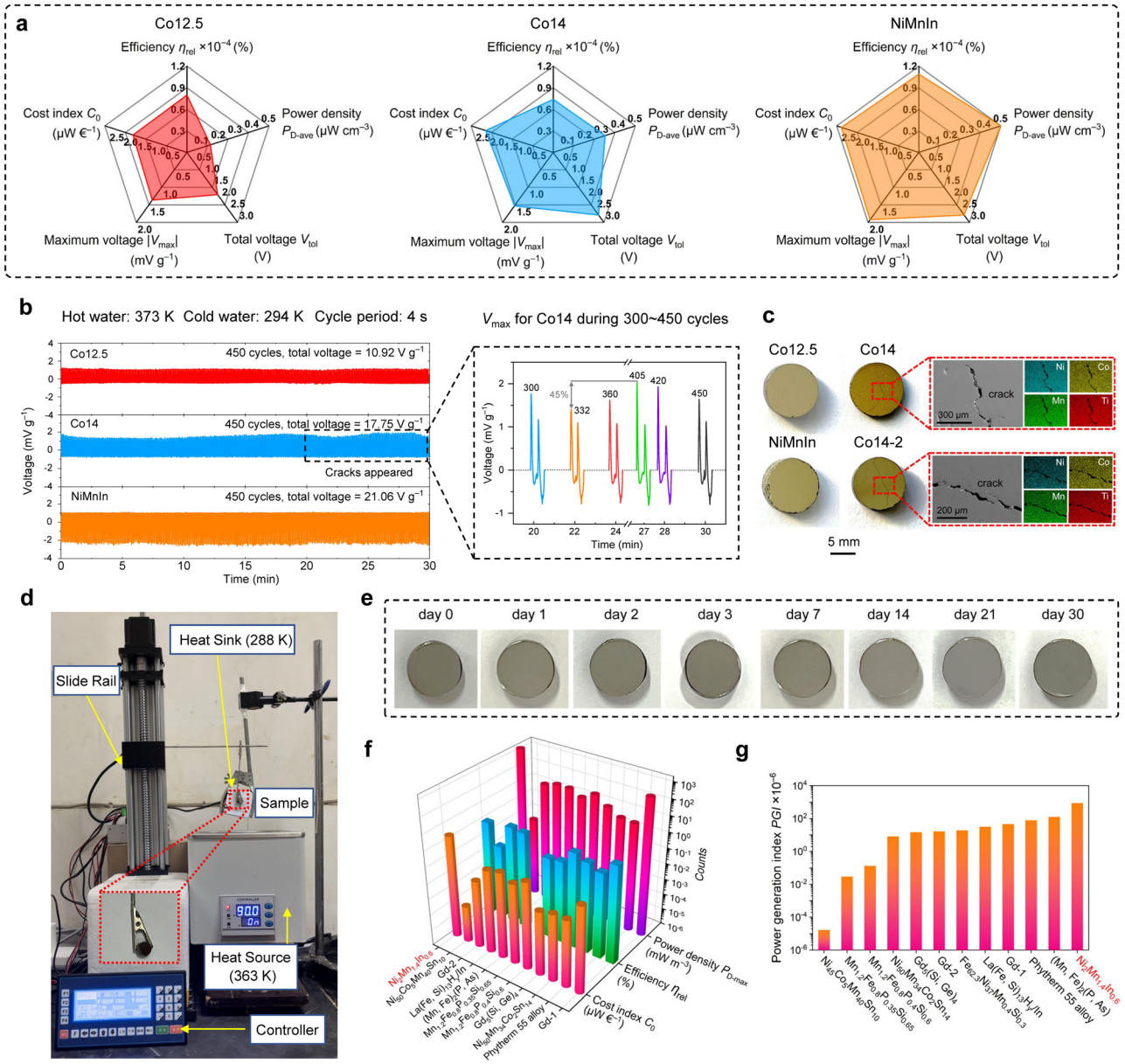

Fig. 4 Comparative analysis of comprehensive TMG performance of Heusler alloys. (a) Comprehensive evaluation of TMG key properties including maximum voltage V_{max}, total voltage V_{tol}, relative energy conversion efficiency η_{rel}, average power density $P_{D\text{-}ave}$, and cost index C_0 for Co12.5, Co14, and NiMnIn, respectively. (b) The induced voltage variation with time for Heusler alloys with different phase transitions within 30 min with a cycle period of 4 s. The enlarged graph shows the increase of V_{max} fluctuation for Co14 with FOMT due to the appearance of cracks after 300 cycles. (c) The surface morphology of all alloys after 450 TMG cycles, and the SEM image and element distribution around the crack of Co14 and Co14-2 alloys. (d) The cycle life test device, and (e) the surface morphology of NiMnIn alloys after 0, 1, 2, 3, 7, 14, 21, and 30 days of heating and cooling cycles. (f) Comprehensive comparison of $P_{D\text{-}max}$, η_{rel}, and C_0 of $Ni_2Mn_{1.4}In_{0.6}$ with other typical TMG materials based on the active TMG devices with a traditional magnetic circuit.[3,24,27,33–37] Note: the η_{rel} of $(Mn, Fe)_2(P, As)$ cannot be calculated since the ΔM and Q_{in} of $(Mn, Fe)_2(P, As)$ are not shown in ref. 33. (g) Comparison of the power generation index PGI of $Ni_2Mn_{1.4}In_{0.6}$ with those of other classic materials based on the active TMG devices with traditional magnetic circuits.[3,24,27,33–37,45]

TMG devices with a traditional magnetic circuit. Fig. 4(f) shows that the $P_{D\text{-}max}$ of NiMnIn is the highest (1752.3 mW m^{-3}), which is 1–5 orders of magnitude higher than those of other classic materials. This fact suggests that NiMnIn alloys could generate larger induced voltage with smaller material volume. Due to the high $P_{D\text{-}max}$ and relatively low raw material cost, $Ni_2Mn_{1.4}In_{0.6}$ shows the highest C_0 of 2.78 μW per €, which is 1–4 orders of magnitude higher than those of other typical reported materials. Besides, NiMnIn also shows a relatively high η_{rel} among these materials.

In addition to above key parameters, we proposed a new systematic comparison index, power generation index (PGI), and it can be calculated using the following equation:

$$\mathrm{PGI} = \frac{I_0}{\Delta T \cdot R \cdot H \cdot \omega} \tag{3}$$

where I_0 is the experimental induced current density, ΔT is the temperature span, R is the total resistance of the system, H is the magnetic field, and ω is the number of coil turns, respectively. The details are shown in Table S2 (ESI†). It can be seen that this PGI index takes into account the factors from both the material and device that influence the induced current, and so the PGI can eliminate the comparison errors caused by various non-intrinsic factors and is more reasonable to compare the TMG performance of different materials. Fig. 4(g) shows the comparison of PGI for SOMT NiMnIn Heusler alloys and other classic materials. The PGI of NiMnIn is 1–7 orders of magnitude higher than those of other typical reported materials.

Consequently, the above comparison result shows that the TMG performance of $Ni_2Mn_{1.4}In_{0.6}$ with SOMT is not only better than those of other two Heusler alloys with different phase transitions, but also better than those of most reported TMG materials. However, it should be noted that only a very small portion of heating/cooling energy can be harvested during the cycling since only a little amount of the sample is used (about 2.5 g). This leads to a low energy conversion efficiency currently for TMG. The Carnot efficiency η_{Carnot} of our TMG device is 21.68%, and the highest η_{rel} is 1.09×10^{-4}%. To improve the efficiency, we can cascade more TMG devices in a circulatory system and use more materials with different phase transition temperatures, which could absorb more thermal energy from the fluid and produce better TMG performance.

3. Conclusions

In summary, in order to study the effect of different phase transitions on the TMG performance, we systematically compared three typical Heusler alloys in the same system with similar composition but different phase transitions based on a lab-built active TMG device. Although both Co12.5 and Co14 alloys generate successive positive and negative V peaks during each heating/cooling cycles due to the FOMT and SOMT, $Ni_2Mn_{1.4}In_{0.6}$ with SOMT presents superior TMG performance due to the large change of magnetization during SOMT and excellent thermal properties. Moreover, the $Ni_2Mn_{1.4}In_{0.6}$ alloy also shows better TMG performance in comparison with other typical TMG materials, *e.g.*, the maximum power density (1752.3 mW m^{-3}) and cost index (2.78 μW per €) of $Ni_2Mn_{1.4}In_{0.6}$ are 1–5 and 1–4 orders of magnitude higher than those of most typical reported materials, respectively. A new comparison parameter (PGI) has been proposed to evaluate the TMG performance more reasonably, and the PGI of NiMnIn is 1–7 orders of magnitude higher than those of other typical reported materials. More importantly, in addition to good TMG performance, $Ni_2Mn_{1.4}In_{0.6}$ with SOMT also shows some advantages that FOMT materials do not have, such as zero magnetic/thermal hysteresis as well as a long-term service life. In contrast to the short lifetime of a few minutes for the materials with FOMT, $Ni_2Mn_{1.4}In_{0.6}$ with SOMT can serve for one month or even longer with excellent cycling stability. Consequently, different from most previous works that emphasized FOMT materials exhibiting high TMG performance, the excellent TMG performance with zero hysteresis and the long-term service life suggest that SOMT NiMnIn Heusler alloys would be better candidates for practical applications of TMG.

4. Experimental section

Materials preparation

$Ni_{37.5}Co_{12.5}Mn_{35}Ti_{15}$ (Co12.5), $Ni_{36}Co_{14}Mn_{35.7}Ti_{14.3}$ (Co14), and $Ni_2Mn_{1.4}In_{0.6}$ (NiMnIn) Heusler alloys were prepared by arc melting or induction-melting of the pure components with a purity higher than 99.2 wt% under an argon atmosphere. The as-cast ingots were sealed in a high-vacuum quartz tube and annealed at 1173 K for 5–7 days, followed by quenching in ice water. The synchrotron radiation X-ray diffraction (XRD) patterns with an energy of 18 kV and a scanning speed of 5° min^{-1} were measured on the BL14B1 beamline at Shanghai Synchrotron Radiation Facility (SSRF).[46] The elemental distribution of the annealed alloys was investigated by energy-dispersive spectroscopy (EDS), as shown in Fig. S18 (ESI†). Moreover, Co12.5, Co14 and NiMnIn were cut into cylindrical pieces of $\varnothing$ 10 × 4 mm *via* wire-cutting. The densities of samples, measured by the Archimedes method, are 7.262 g cm^{-3}, 7.217 g cm^{-3}, and 7.935 g cm^{-3} for Co12.5, Co14, and NiMnIn, respectively.

Microstructure characterization

The differential scanning calorimetry (DSC) measurements were carried out using a DSC 6220 with a heating/cooling rate of 10 K min^{-1}. The microstructure was studied using a Merlin VP Compact field emission scanning electron microscope (SEM), and the elemental analysis was performed by energy-dispersive spectroscopy (EDS). The room temperature high-resolution transmission electron microscopy (HRTEM) images, selected area electron diffraction (SAED) patterns, and the *In situ* TEM images at different temperatures were obtained using a JEM-2100F transmission electron microscope (TEM) from Japan Electronics Co., Ltd (JEOL).

Magnetic and thermal properties

The magnetization and specific heat were measured using a cryogen-free cryocooler-based physical property measurement system (model VersaLab) from Quantum Design Inc. The magnetization isotherms were measured by adopting a loop process. The thermal conductivity (λ) was determined by utilizing the thermal transport option of the platform, at a heating/cooling rate of ±0.2 K min^{-1}.

Fabrication of the TMG device

The structure and working mechanism of our lab-built active TMG device are shown in Fig. 1. A 3D printed nylon shell is placed in a hollow cylindrical Halbach permanent magnet which provides a radial magnetic field of ~1 T. The copper cabin passes through the center of the nylon shell, which is

wound by 600 turns of copper coil. The resistance of the copper measured using a multimeter is 6.7 Ω. Ice water (~273 K) and boiling water (~373 K), acting as cold and hot sources, were pumped alternatively to flow through the sample cabin at a flow rate of 0.04 L s^{-1} controlled by a programmed microcontroller. Two thermocouples are placed in the ice water and hot water buckets to measure the temperature, so that we can keep the temperature constant by adding more ice or boiling water timely. The temperature of the sample surface was measured with a K-type thermocouple placed on the surface of the sample. Since the measured surface temperature cannot accurately represent the average temperature of the bulk sample due to its internal temperature gradient, the average temperature (T_{ave}) of the sample was calculated using the isometric segmentation method (Fig. S7, ESI†). The infrared images during the operation of the TMG were captured with an infrared imager (Testo 890), and the image is processed using IRsoft published by Testo Inc (Fig. S11, ESI†). The induced electrical signal and temperature data were collected by using a data collection system (RIGOL M300), and the induced voltage value was divided by the resistance value to obtain the induced current.

Finite element simulations

Finite element simulations were carried out with the COMSOL Multiphysics software (Version 5.4). We used the heat transfer module and magnetic field module to simulate the temperature change of the TMG materials and the induced voltage generated by TMG. The specific modeling and simulation process are described in ESI,† Note 6. The simulated results were compared with the experimental results.

Data availability

The data sets generated and analyzed during the current study are available from the corresponding author upon reasonable request.

Author contributions

H. Z. conceived the project. H. D. C. carried out the main experiments and wrote the original draft. X. L. L. performed the finite element simulations. Y. L. carried out the microstructure characterization. L. L. X. and M. Z. L. measured the TMG properties. Z. Y. Y. and K. M. Q. performed the magnetic measurements. F. X. H., B. G. S., R. V. R., and K. C. discussed the results and reviewed the manuscript. H. D. C. and H. Z. prepared the manuscript with contributions from all authors.

Conflicts of interest

The authors declare no competing interests.

Acknowledgements

This work was supported by the National Natural Science Foundation of China (grant no. 52171169, 52101210, and 52088101), the National Key Research and Development Program of China (grant no. 2021YFB3501204, 2020YFA0711502), the China Postdoctoral Science Foundation (grant no. 2021M690346), and the State Key Laboratory for Advanced Metals and Materials (grant no. 2023-ZD01). This research is partially supported by grants from the National Research Foundation, Prime Minister's Office, Singapore under its Campus of Research Excellence and Technological Enterprise (CREATE) programme.

Notes and references

1 G. Schierning, *Nat. Energy*, 2018, **3**, 92–93.
2 P. Kumar, R. A. Kishore, D. Maurya, C. J. Stewart, R. Mirzaeifar, E. Quandt and S. Priya, *Appl. Energy*, 2019, **251**, 113277.
3 H. Chen, Z. Ma, X. Liu, K. Qiao, L. Xie, Z. Li, J. Shen, W. Dai, Z. Ou, H. Yibole, O. Tegus, S. V. Taskaev, K. Chu, Y. Long and H. Zhang, *Appl. Energy*, 2022, **306**, 117999.
4 C. Forman, I. K. Muritala, R. Pardemann and B. Meyer, *Renewable Sustainable Energy Rev.*, 2016, **57**, 1568–1579.
5 M. Langan and K. O'Toole, *Energy Procedia*, 2017, **123**, 188–195.
6 T. Y. Kim, J. Kwak and B.-W. Kim, *Energy Convers. Manage.*, 2018, **160**, 14–21.
7 J. Choi, K. Cho, J. Yun, Y. Park, S. Yang and S. Kim, *Adv. Energy Mater.*, 2017, **7**, 1700972.
8 D. Vuarnoz, A. Kitanovski, C. Gonin, Y. Borgeaud, M. Delessert, M. Meinen and P. W. Egolf, *Appl. Energy*, 2012, **100**, 229–237.
9 A. Chiolerio, E. Garofalo, F. Mattiussi, M. Crepaldi, G. Fortunato and M. Iovieno, *Appl. Energy*, 2020, **277**, 115591.
10 M. Bevione, E. Garofalo, L. Cecchini and A. Chiolerio, *MRS Energy Sustain.*, 2020, **7**, 1–10.
11 C. Cai, B. Luo, Y. Liu, Q. Fu, T. Liu, S. Wang and S. Nie, *Mater. Today*, 2022, **52**, 299–326.
12 S. Chatterjee, S. R. Burman, I. Khan, S. Saha, D. Choi, S. Lee and Z.-H. Lin, *Nanoscale*, 2020, **12**, 17663–17697.
13 K. Deepak, V. B. Varma, G. Prasanna and R. V. Ramanujan, *Appl. Energy*, 2019, **233–234**, 312–320.
14 R. A. Kishore, B. Davis, J. Greathouse, A. Hannon, D. Emery Kennedy, A. Millar, D. Mittel, A. Nozariasbmarz, M. G. Kang, H. B. Kang, M. Sanghadasa and S. Priya, *Energy Environ. Sci.*, 2019, **12**, 1008–1018.
15 M. Gueltig, H. Ossmer, M. Ohtsuka, H. Miki, K. Tsuchiya, T. Takagi and M. Kohl, *Adv. Energy Mater.*, 2014, **4**, 1400751.
16 J. Joseph, M. Ohtsuka, H. Miki and M. Kohl, *Joule*, 2020, **4**, 2718–2732.
17 M. Lallart, L. Yan, H. Miki, G. Sebald, G. Diguet, M. Ohtsuka and M. Kohl, *Appl. Energy*, 2021, **288**, 116617.
18 J. Joseph, E. Fontana, T. Devillers, N. M. Dempsey and M. Kohl, *Adv. Funct. Mater.*, 2023, **33**, 2301250.

19 Z. Xu, R. Wang and C. Yang, *Energy*, 2019, **176**, 1037–1043.
20 N. Tesla, *US Pat.*, 428057, 1890.
21 T. A. Edison, *US Pat.*, 476983, 1892.
22 O. Tegus, E. Brück, K. Buschow and F. Boer, *Nature*, 2002, **415**, 150–152.
23 J. Liu, T. Gottschall, K. P. Skokov, J. D. Moore and O. Gutfleisch, *Nat. Mater.*, 2012, **11**, 620–626.
24 V. Srivastava, Y. Song, K. Bhatti and R. D. James, *Adv. Energy Mater.*, 2011, **1**, 97–104.
25 A. Waske, D. Dzekan, K. Sellschopp, D. Berger, A. Stork, K. Nielsch and S. Fähler, *Nat. Energy*, 2018, **4**, 68–74.
26 K. Deepak, M. S. Pattanaik and R. V. Ramanujan, *Appl. Energy*, 2019, **256**, 113917.
27 Z. Ma, H. Chen, X. Liu, C. Xing, M. Wu, Y. Wang, P. Liu, Z. Ou, J. Shen, S. V. Taskaev, K. Long, Y. Long and H. Zhang, *Adv. Sustainable Syst.*, 2021, **5**, 2000234.
28 J. Joseph, M. Ohtsuka, H. Miki and M. Kohl, *iScience*, 2022, **25**, 104569.
29 M. Gueltig, F. Wendler, H. Ossmer, M. Ohtsuka, H. Miki, T. Takagi and M. Kohl, *Adv. Energy Mater.*, 2017, **7**, 1601879.
30 H. Miki, E. Abe, S. Takeda, M. Ohtsuka and M. Kohl, *Sens. Mater.*, 2020, **32**, 2867–2875.
31 S. Singh, L. Caron, S. W. D'Souza, T. Fichtner, G. Porcari, S. Fabbrici, C. Shekhar, S. Chadov, M. Solzi and C. Felser, *Adv. Mater.*, 2016, **28**, 3321–3325.
32 X. Liu, H. Chen, J. Huang, K. Qiao, Z. Yu, L. Xie, R. V. Ramanujan, F. Hu, K. Chu, Y. Long and H. Zhang, *Nat. Commun.*, 2023, **14**, 4811.
33 T. Christiaanse and E. Brück, *Metall. Mater. Trans. E*, 2014, **1**, 36–40.
34 M. Lallart, L. Wang, G. Sebald, L. Petit and D. Guyomar, *Phys. Lett. A*, 2014, **378**, 3151–3154.
35 X. Liu, H. Zhang, H. Chen, Z. Ma, K. Qiao, L. Xie, Z. Ou, J. Wang, F. Hu and B. Shen, *Appl. Therm. Eng.*, 2023, **221**, 119827.
36 L. Bi, O. Tegus, R. Yi and H. Shi, *Acta Phys. Sin.*, 2012, **61**, 077103.
37 Z. Liu, O. Tegus, Z. Ou, W. Fan, Z. Song, H. Lu, W. Wei and R. Han, *Acta Phys. Sin.*, 2015, **64**, 047103.
38 Z. Wei, E. Liu, J. Chen, Y. Li, G. Liu, H. Luo, X. Xi, H. Zhang, W. Wang and G. Wu, *Appl. Phys. Lett.*, 2015, **107**, 022406.
39 Y. Qu, A. Gràcia-Condal, L. Mañosa, A. Planes, D. Cong, Z. Nie, R. Yang and Y. Wang, *Acta Mater.*, 2019, **177**, 46–55.
40 W. Sun, X. Lu, Z. Wei, Q. Li, Z. Li, Y. Zhang and J. Liu, *Addit. Manuf.*, 2022, **59**, 103125.
41 H. Neves Bez, A. K. Pathak, A. Biswas, N. Zarkevich, V. Balema, Y. Mudryk, D. D. Johnson and V. K. Pecharsky, *Acta Mater.*, 2019, **173**, 225–230.
42 K. Liu, X. Han, K. Yu, C. Ma, Z. Zhang, Y. Song, S. Ma, H. Zeng, C. Chen, X. Luo, S. U. Rehman and Z. Zhong, *Intermetallics*, 2019, **110**, 106472.
43 T. Krenke, E. Duman, M. Acet, E. F. Wassermann, X. Moya, L. Manosa and A. Planes, *Nat. Mater.*, 2005, **4**, 450–454.
44 D. Dzekan, A. Waske, K. Nielsch and S. Fähler, *APL Mater.*, 2021, **9**, 011105.
45 J. Liu, Y. Long, D. Bai, H. Sun, H. Zhang, K. Long and T. Yan, *AIP Adv.*, 2019, **9**, 045227.
46 T. Yang, W. Wen, G. Yin, X. Li, M. Gao, Y. Gu, L. Li, Y. Liu, H. Lin and X. Zhang, *Nucl. Technol.*, 2015, **26**, 20101.

